Negative-U carbon vacancy in 4H-SiC: Assessment of charge correction schemes and identification of the negative carbon vacancy at the quasicubic site

X. T. Trinh,[1] K. Szász,[2,3] T. Hornos,[2] K. Kawahara,[4] J. Suda,[4] T. Kimoto,[4] A. Gali,[2,5,*] E. Janzén,[1] and N. T. Son[1,†]

[1]*Department of Physics, Chemistry and Biology, Linköping University, SE-581 83 Linköping, Sweden*

[2]*Institute for Solid State Physics and Optics, Wigner Research Centre for Physics, Hungarian Academy of Sciences, P.O. Box 49, H-1525 Budapest, Hungary*

[3]*Institute of Physics, Loránd Eötvös University, Pázmány Péter sétány 1/A, H-1117 Budapest, Hungary*

[4]*Department of Electronic Science and Engineering, Kyoto University, Nishikyo, Kyoto 615-8510, Japan*

[5]*Department of Atomic Physics, Budapest University of Technology and Economics, Budafoki út 8, H-1111 Budapest, Hungary*

(Received 6 June 2013; published 26 December 2013)

The carbon vacancy (V_C) has been suggested by different studies to be involved in the Z_1/Z_2 defect-a carrier lifetime killer in SiC. However, the correlation between the Z_1/Z_2 deep level with V_C is not possible since only the negative carbon vacancy (V_C^-) at the hexagonal site, $V_C^-(h)$, with unclear negative-U behaviors was identified by electron paramagnetic resonance (EPR). Using freestanding n-type 4H-SiC epilayers irradiated with low energy (250 keV) electrons at room temperature to introduce mainly V_C and defects in the C sublattice, we observed the strong EPR signals of $V_C^-(h)$ and another $S = 1/2$ center. Electron paramagnetic resonance experiments show a negative-U behavior of the two centers and their similar symmetry lowering from C_{3v} to C_{1h} at low temperatures. Comparing the ^{29}Si and ^{13}C ligand hyperfine constants observed by EPR and first principles calculations, the new center is identified as $V_C^-(k)$. The negative-U behavior is further confirmed by large scale density functional theory supercell calculations using different charge correction schemes. The results support the identification of the lifetime limiting Z_1/Z_2 defect to be related to acceptor states of the carbon vacancy.

I. INTRODUCTION

Silicon carbide (SiC) has long been considered as an attractive material for high-voltage power devices.[1,2] For a blocking voltage higher than several kilovolts for very high-voltage applications, such as electric power transmission, bipolar devices have great advantages in terms of lower on-resistance owing to the effect of conductivity modulation.[3] In such high-voltage power devices, a long carrier lifetime is required for effective modulation of the conductivity of very thick blocking-voltage layers. For example, a lifetime longer than 5 μs will be required for effective conductivity modulation in 10 kV SiC PiN diodes.

Currently, the carrier lifetime in high-purity as-grown SiC epitaxial layers is rather short (typically less than ~2 μs). It was suggested by different studies[4–8] that the carrier lifetime in bulk 4H-SiC is limited by the Z_1/Z_2 deep level located at ~0.65 eV below the conduction band minimum (CBM) (~$E_C - 0.65$ eV).[9,10] Since the Z_1/Z_2 defect is always present in as-grown material[10] and has strong influence on device applications of SiC, there has been considerable effort in identification and elimination of the defect. Studies of SiC irradiated by low-energy (<250 keV) electrons, which can mainly replace C atoms and, hence, create defects in the C sublattice, suggested that the Z_1/Z_2 defect is related to the C vacancy (V_C) (with either monovacancy or V_C-related complexes).[11,12] The Z_1/Z_2 center is also known to be a negative-U system, having higher lying excited states Z_1 (at ~$E_C - 0.52$ eV) and Z_2 (at ~$E_C - 0.45$ eV) in 4H-SiC.[13] The correlation between Z_1/Z_2 and the EH_7 center at ~$E_C - (1.55/1.65)$ eV (Refs. 12 and 14) in the formation, concentration, and annealing behavior observed in different types of materials suggested that the two centers belong to the same defect.[12] It

has been shown that the concentration of Z_1/Z_2 and EH_7 in thick layers can be efficiently reduced by C implantation and subsequent annealing[15,16] or thermal oxidation,[17,18] supporting the suggestion that these centers are V_C-related.

The carbon vacancy in SiC has been predicted to have low formation energies and should be abundant in materials grown in either Si-rich or C-rich conditions.[19,20] In SiC, different charge states of V_C, from the double positive 2+ to double negative 2− charge states, are within the band gap.[19–21] In the single positive charge state (V_C^+), the defect has an electron spin $S = 1/2$ and has been identified by electron paramagnetic resonance (EPR) in 4H- and 6H-SiC.[22–26] In 4H-SiC, the $(+|0)$ single donor level of V_C was estimated by photoexcitation EPR (photo-EPR) to be at ~$E_C - (1.8–1.9)$ eV.[27–29] The V_C^+ center is a common defect in high-purity semi-insulating (HPSI) SiC substrates[30–33] and is suggested to be related to the $EH_{6/7}$ center.[29,34] The V_C defect has been used for controlling the resistivity in commercial HPSI SiC substrates,[35,36] although the detailed mechanism of carrier compensation involving the C vacancy is still not clear. Among different intrinsic defects, V_C and the divacancy have been suggested to be the most suitable defects for obtaining thermally stable semi-insulating properties in HPSI SiC substrates.[34] The negative V_C center (V_C^-) has also been identified in n-type 4H-SiC substrates irradiated by high-energy (2 MeV) electrons at 850 °C (Ref. 37). However, only V_C^- at the hexagonal lattice site, $V_C^-(h)$, has been identified.[37] In a later EPR study of low-doped (the N concentration [N] ~ 7 × 10^{14} cm^{-3}) n-type 4H-SiC epilayers irradiated by 200 keV electrons, only a weak signal of the $V_C^-(h)$ signal was detected.[29] In those EPR studies,[29,37] the 2-level of V_C was estimated to be at ~1.0–1.1 eV below the CBM, and no clear negative-U properties have been observed. Calculations by

Torpo and co-workers[20] suggested a positive-U behavior for V_C with the double and single negative charge states located closely at $\sim$1.1–1.2 eV below the CBM. More recent hybrid functional calculations[21] showed the acceptor levels of V_C to be very close to the ionization energy of the Z_1/Z_2 center, but the negative-U behavior was found only for V_C^- at the quasicubic site, $V_C^-(k)$.

Recently, using relatively high-doped ([N] $\sim$ 1.6 $\times$ 10^{17} cm^{-3}) n-type epilayers irradiated by 250 keV electrons, it was possible to perform EPR, deep level transient spectroscopy (DLTS), and capacitance versus voltage (C-V) measurements on samples irradiated with the same fluences.[38,39] In those irradiated layers, the EPR signals of $V_C^-(h)$ and a new spectrum were dominating. However, since the layers were irradiated only on one side with the penetration depth of $\sim$45 μm, the strong EPR signals of the N shallow donors in the unirradiated part prevent the study at low temperatures. The correlation between EPR, which was performed at high temperatures (>100 K) when the symmetry had already changed to C_{3v}, and calculations of V_C^- at low temperatures with C_{1h} symmetry was not possible.[38] Therefore, the new spectrum was assumed to be $V_C^-(k)$ based on the similarity between the two centers in the formation and spin-Hamiltonian parameters determined at high temperatures.

In the present study, electron irradiation was performed on both sides of the layers. With the electron fluence of $\sim$7.5 $\times$ 10^{18} cm^{-2}, the layers show no EPR signals of the N shallow donors at low temperatures in darkness. This allows us to study the temperature dependence of the V_C^- signal, revealing the negative-U behavior of both the $V_C^-(h)$ and $V_C^-(k)$ centers, and to observe the ligand hyperfine (hf) structures of the vacancies at low temperatures in their low symmetry configurations without interference from other EPR signals. The Si and C ligand hf constants observed by EPR at low temperatures can be directly compared to that determined by supercell calculations. The charge transition levels of the carbon vacancies in $4H$-SiC were also investigated in large supercells and compared to the experiments. In this investigation, the assessment of different charge correction techniques of the supercell model was carried out.

II. EXPERIMENT

The starting materials were n-type $4H$-SiC epitaxial layers grown by chemical vapor deposition with different nitrogen concentrations of [N] $\sim$ 1 $\times$ 10^{14} cm^{-3} and [N] $\sim$ 1.6 $\times$ 10^{17} cm^{-3}. The substrates were removed by polishing, and the freestanding layers with a thickness of $\sim$100 μm were irradiated by 250 keV electrons at room temperature to a fluence of $\sim$7.5 $\times$ 10^{18} cm^{-2}. In high-doped layers, this electron fluence creates a compensated region of 45 μm thick, where the N shallow donor is completely compensated. In this compensated region, the Fermi level is located at $\sim E_C -$ 0.53 eV (Ref. [39]). In order to compensate the whole layers to avoid the interference of the EPR signal of the N shallow donors at low temperatures (below 100 K), both sides of the layers were irradiated. EPR experiments were performed on a Bruker X-band ($\sim$9.42 GHz) E500 spectrometer equipped with a He-flow cryostat, which allows the regulation of the sample temperature in the range of 4–295 K. For optical

excitation, a 200 W halogen lamp, appropriate filters, and a Jobin-Yvon 0.25-m single-grating monochromator were used as a light source. With fully open slits of the monochromator and using the second order of a 600 g/mm grating, the error in the photon energy is $\sim$6 meV and $\sim$10 meV in the near-infrared and visible spectral regions, respectively, and the corresponding errors in determination of the energy threshold can be $\sim$10 meV and $\sim$20 meV.

III. RESULTS AND DISCUSSION

A. EPR spectra and analysis

In low-doped ([N] $\sim$ 1 $\times$ 10^{14} cm^{-3}) irradiated layers, only the broad EPR signal of the SI-1 defect[31] was observed in darkness. Figure 1(a) shows the spectrum in a low-doped, heavily irradiated ($\sim$7.5 $\times$ 10^{18} electrons/cm^2) sample measured in darkness at 100 K for the magnetic field **B** along the c axis (**B**∥**c**). Under illumination with the light of photon energies of $h\nu \sim$ 1.81 eV, four EPR lines appear. The intensity of these lines increases with increasing photon energy and reaches the maximum when $h\nu \sim$ 3 eV [Fig. 1(b)]. From the g values and their hf A-tensors, these EPR signals are recognized to be related to $V_C^+(k)$, $V_C^+(h)$ (Ref. [23]), and $V_C^-(h)$ (Ref. [37]). In addition to these known spectra, a new EPR line at $\sim$335.54 mT was observed, as can be seen in the inset of Fig. 1 with an extended magnetic field scale. Only these four
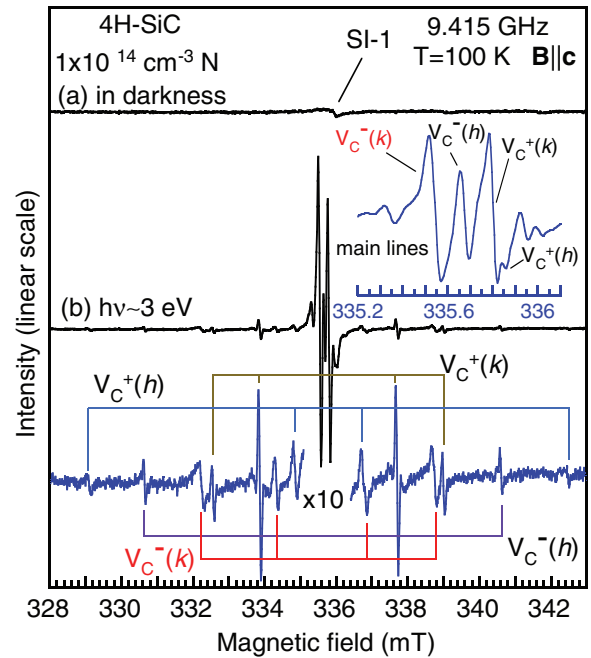

FIG. 1. (Color online) EPR spectra in low-doped ([N] $\sim$ 1 $\times$ 10^{14} cm^{-3}) n-type $4H$-SiC layer irradiated by 250 keV electrons to a fluence of $\sim$7.5 $\times$ 10^{18} cm^{-2} measured for **B**∥**c** at 100 K. (a) In darkness, only a weak signal of the SI-1 defect (Ref. [31]) can be observed, whereas (b) under illumination with light of photon energies $h\nu \sim$ 3 eV, strong signals of $V_C^+(k)$, $V_C^+(h)$, $V_C^-(h)$, and a new signal, which we will show later to be related to $V_C^-(k)$, were observed. Their main lines are shown in the inset and their hf structures are shown in $\times$10 intensity-scale spectrum.
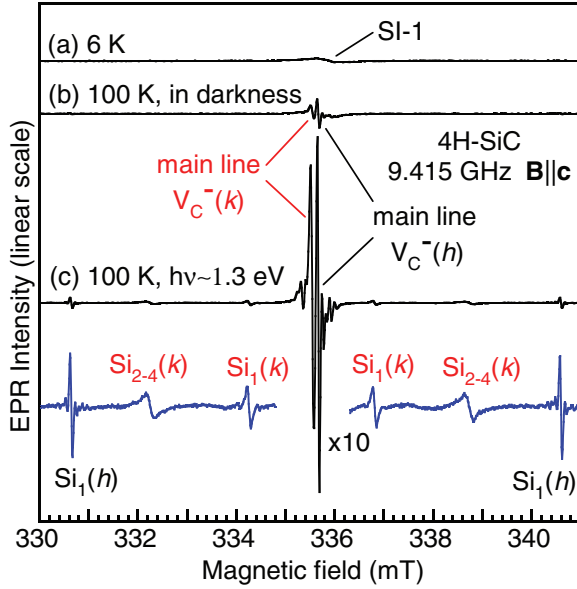
FIG. 2. (Color online) EPR spectra in a high-doped ([N] $\sim 1.6 \times 10^{17}$ cm^{-3}) n-type 4H-SiC layer irradiated by 250 keV electrons to a fluence of $\sim 7.5 \times 10^{18}$ cm^{-2} measured for **B**∥**c** at (a) 6 K and (b) 100 K in darkness and (c) at 100 K under illumination with light of photon energies $h\nu \sim 1.3$ eV. The hf structures of $V_C^-(k)$ and $V_C^-(h)$ are shown in $\times 10$ intensity-scale spectrum. The weak and broad signal at 6 K is from the SI-1 center (Ref. 31).
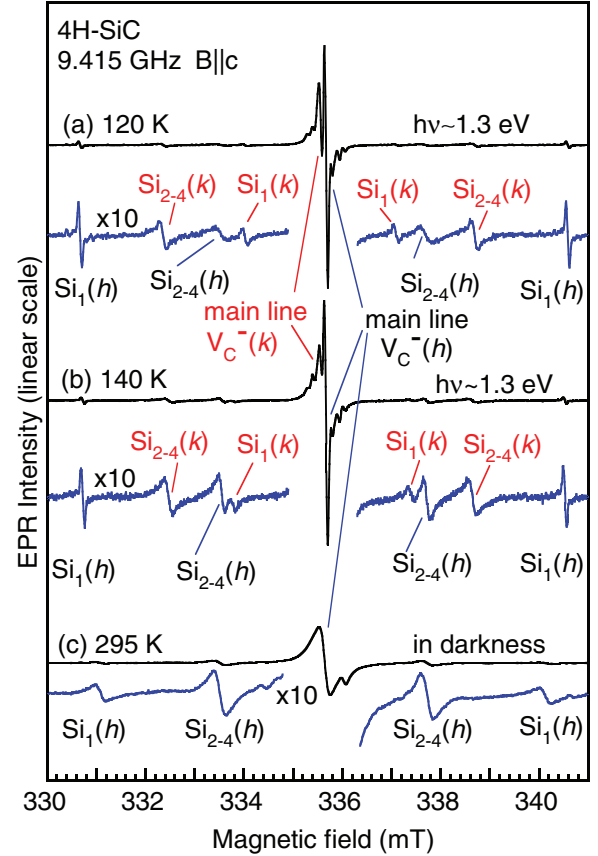

FIG. 3. (Color online) EPR spectra in a high-doped n-type 4H-SiC layer irradiated by 250 keV electrons to a fluence of $\sim 7.5 \times 10^{18}$ cm^{-2} measured for **B**∥**c** with low microwave (MW) power (0.1 mW) under illumination with light of photon energies $h\nu \sim 1.3$ eV at (a) 120 K and (b) 140 K. (c) The EPR spectrum of $V_C^-(h)$ measured for **B**∥**c** at 295 K with high MW power (63.25 mW) showing the Si hf structure due to hf interaction with one ^{29}Si atom occupying one of four nearest Si sites.

EPR centers were detected in irradiated layers. Since two of them are related to V_C^+ at two inequivalent lattice sites and the third line is from $V_C^-(h)$, it is naturally expected that the fourth line is from V_C^- at the quasicubic site (k site). We therefore label this signal as $V_C^-(k)$ and show our results below.

The EPR spectrum in high-doped ([N] $\sim 1.6 \times 10^{17}$ cm^{-3}) irradiated samples measured in darkness at 6 K also shows only the SI-1 signal [Fig. 2(a)]. The $V_C^-(h)$ signal appeared when the temperature reaches ~ 85 K. At ~ 100 K, the $V_C^-(k)$ signal is weakly observed. At temperatures lower than ~ 80 K, the observation of these signals requires illumination with the light of photon energies $h\nu \geq 0.74$–0.78 eV. The intensity of both lines reaches the maximum when the photon energies are $h\nu \sim 1.3$ eV or larger. The $V_C^-(h)$ and $V_C^-(k)$ main lines and their hf structures were measured at 100 K under illumination with photon energy of $h\nu \sim 1.3$ eV [Fig. 2(c)]. At this temperature, the $V_C^-(h)$ spectrum showed the hf structure due to the hf interaction between the electron spin and the nuclear spin of one nearest ^{29}Si ($I = 1/2$, natural abundance 4.67%) neighbor along the c axis, labeled Si$_1(h)$, in agreement with previous results.[37] For $V_C^-(k)$, two pairs of weak satellites were observed [Fig. 2(c)]. The inner and outer pairs have intensity ratios with the main line of $\sim 5\%$ and $\sim 15\%$, which are approximately the natural abundance of one and three ^{29}Si, respectively; therefore, they are assigned to the hf structures due to the hf interaction between the electron spin and the nuclear spin of one ^{29}Si atom occupying the nearest Si site along the c axis, labeled as Si$_1(k)$, and the three nearest Si sites in the basal plane, labeled Si$_{2-4}(k)$, respectively.

In our samples, the $V_C^-(h)$ and $V_C^-(k)$ signals seem to be strongest at ~ 100 K under illumination. However, at this temperature, the hf lines of $V_C^-(k)$ are broad. With increasing temperature, these hf lines become narrower, and another hf structure of $V_C^-(h)$, labeled Si$_{2-4}(h)$, appears. Figure 3(a) shows the hf structures of $V_C^-(h)$ and $V_C^-(k)$ measured at 120 K for **B**∥**c** under illumination with light of photon energies $h\nu \sim 1.3$ eV. At ~ 140 K, these hf lines get even narrower [Fig. 3(b)]. The Si$_{2-4}(h)$ hf lines were not reported in the previous study by Umeda *et al.*[37] At temperatures above ~ 250 K, the $V_C^-(k)$ signal becomes very weak and cannot be detected, whereas the $V_C^-(h)$ signal can still be observed at room temperature. Figure 3(c) shows the $V_C^-(h)$ spectrum and its hf structure due to the hf interaction between the electron spin and the nuclear spin of one ^{29}Si atom occupying one of the four nearest Si sites measured in darkness at 295 K for **B**∥**c**.

The angular dependence of the magnetic field positions of EPR lines measured at 140 K with the magnetic field **B** rotating in the (1$\bar{1}$00) plane is shown as open circles in Fig. 4. The main lines of $V_C^-(h)$ and $V_C^-(k)$ do not split, showing C_{3v} symmetry of the centers. In order to distinguish between the C_{3v} and C_{1h} configurations of these defects, we label these C_{3v} centers
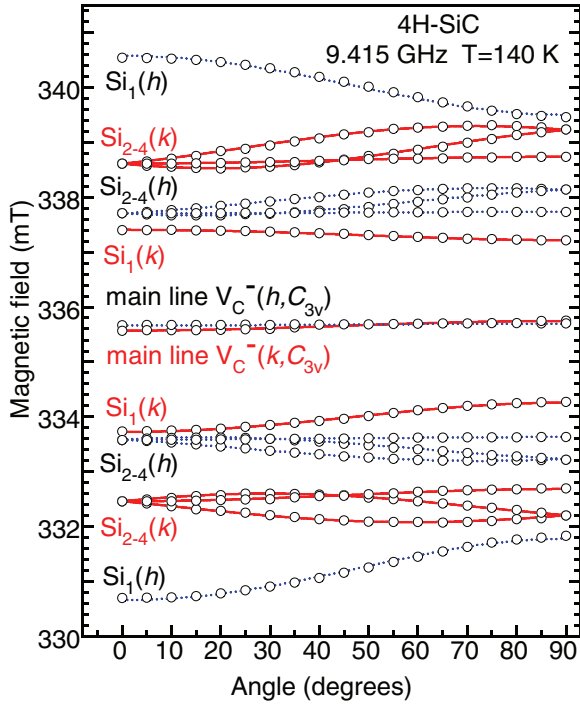
FIG. 4. (Color online) Angular dependence of the magnetic field positions of EPR lines (open circles) measured at 140 K with **B** rotating in the $(1\bar{1}00)$ plane. The solid and dashed curves represent the simulated angular dependences for $V_C^-(k, C_{3v})$ and $V_C^-(h, C_{3v})$, respectively, using Eq. (1) and parameters in Table I. The angle $0°$ and $90°$ correspond to the directions $\mathbf{B}\|\mathbf{c}$ and $\mathbf{B}\perp\mathbf{c}$, respectively.

as $V_C^-(h, C_{3v})$ and $V_C^-(k, C_{3v})$. The angular dependences of the magnetic field positions of the $Si_1(h)$ and $Si_1(k)$ hf lines show C_{3v} symmetry, as expected for the Si atom along the c axis. As can be seen in the figure, when rotating the magnetic field away from the c axis, the $Si_{2-4}(h)$ and $Si_{2-4}(k)$ hf lines, each splits into three lines, showing a typical rotation pattern of C_{1h} symmetry. The angular dependence of the magnetic field positions of the main lines and hf lines of $V_C^-(h, C_{3v})$ and $V_C^-(k, C_{3v})$ at 140 K can be described by the following spin-Hamiltonian:

$$H = \mu_B \mathbf{g}.\mathbf{B}.\mathbf{S} + \sum_i \mathbf{S}.\mathbf{A}_i.\mathbf{I}. \qquad (1)$$

Here μ_B is the Bohr magneton and the spin $S = 1/2$ and $I = 1/2$. The g-tensor has its usual meaning and is constrained to C_{3v} symmetry, and $\mathbf{A}_i$ are the hf tensors representing hf interactions with four nearest Si neighbors, $Si_1(h)$, $Si_{2-4}(h)$, $Si_1(k)$, and $Si_{2-4}(k)$, of $V_C^-(h, C_{3v})$ and $V_C^-(k, C_{3v})$. The principal values of the g- and A-tensors at 140 K obtained from the best fits are given in Table I. As expected, the principal values of the g-tensor of $V_C^-(h, C_{3v})$ and A-tensor of $Si_1(h)$ obtained from the fits are very similar to those reported before for $V_C^-(h, C_{3v})$ determined at 150 K (Ref. 37). The simulated angular dependences of the magnetic field positions of the $V_C^-(h, C_{3v})$ and $V_C^-(k, C_{3v})$ lines using the obtained spin-Hamiltonian parameters and Eq. (1) are plotted as dotted and solid curves, respectively, in Fig. 4.

The angular dependence of the magnetic field positions of $V_C^-(h, C_{3v})$ lines measured at 295 K with the magnetic field rotating in the $(1\bar{1}00)$ plane is shown as open circles in Fig. 5. The principal values of the g- and A-tensors obtained from the fits using the spin-Hamiltonian Eq. (1) are also given in Table I. As can be seen in Table I, with increasing temperature from 140 K to 295 K, $V_C^-(h, C_{3v})$ shows a negligible change in the g values, but its principal A values slightly decrease for $Si_1(h)$ and increases for $Si_{2-4}(h)$. The simulated angular dependence using the obtained parameters is plotted as solid curves in Fig. 5.

It is known from previous study of $V_C^-(h)$ that the thermally activated reorientation occurs in the temperature range of 60–80 K (Ref. 37). This causes the broadening of the hf $Si_2(h)$ lines. Similar line broadening is also observed for the $Si_{2-4}(k)$ hf lines of $V_C^-(k)$. With reducing temperature from 140 K to $\sim$80 K, the $Si_{2-4}(k)$ hf lines are broadened and disappeared, whereas the $Si_1(k)$ hf lines show the same linewidth, but their hf splitting is drastically reduced, e.g., the splitting at the c direction is $\sim$3.69 mT at 140 K [Fig. 3(b)], $\sim$2.52 mT at 100 K [Fig. 2(c)], $\sim$2 mT at 90 K, and $\sim$1 mT at $\sim$60 K [Figs. 6(a)–6(c)]. At $\sim$40 K, the $Si_1(k)$ hf lines could not be observed, and three new pairs of hf lines of $V_C^-(k)$ appear [Fig. 6(d)]. The signals get stronger and narrower at $\sim$30 K [Fig. 6(e)]. At this temperature and under low-power illumination, the $V_C^-(h)$ signal reduces to the noise level, and only lines from $V_C^-(k)$ are seen in the spectrum [Fig. 6(f)]. The largest splitting hf lines of $V_C^-(k)$ have the total intensity of $\sim$10% of the main line and are, therefore, assigned to be related to the hf interaction between the electron spin and the nuclear spin of one ^{29}Si atom occupying one of two nearest Si sites, labeled as $Si_{3,4}(k)$. The strong and weak inner hf lines have intensity ratios with the main line of $\sim$10% and $\sim$2.5%, respectively [Figs. 6(e) and 6(f)], and are assigned to be the hf structures due to the hf interaction between the electron spin and the nuclear spin of one ^{29}Si atom occupying one of two Si sites, labeled as $Si_{5,6}(k)$, and of one ^{13}C atom ($I = 1/2$ and a natural abundance of $\sim$1.1%) at two C sites, labeled as $C_{1,2}(k)$, respectively. The neighbor sites of $Si_{5,6}(k)$ and $C_{1,2}(k)$ will be described later with the help of first principles simulations.

Since the parameters of $V_C^-(h)$ at 60 K have already been determined,[37] we present here only the angular dependence study of $V_C^-(k)$. In order to avoid the interference from the signal of $V_C^-(h)$, the study was performed at 30 K. The angular dependence of the magnetic field positions of $V_C^-(k)$ lines with the magnetic field rotating in the $(1\bar{1}00)$ plane measured at 30 K is shown in Fig. 7. As can be seen in the figure, at an arbitrary direction the main line splits into three lines, indicating the symmetry lowering to C_{1h} similar to the $V_C^-(h)$ center.[37] We label these C_{1h} configurations of V_C^- at low temperatures as $V_C^-(k, C_{1h})$ and $V_C^-(h, C_{1h})$. The $Si_{5,6}(k)$, $C_{1,2}(k)$, and $Si_{3,4}(k)$ hf lines each split into six lines corresponding to six possible defect orientations (with respect to the direction of magnetic field), indicating their lowest symmetry C_1 in a hexagonal lattice. Analyzing the obtained angular dependences using the spin-Hamiltonian Eq (1), we obtain the g-tensor for $V_C^-(k, C_{1h})$ and the hf A-tensors for $Si_{5,6}(k)$, $C_{1,2}(k)$, and $Si_{3,4}(k)$. The obtained parameters are given in Table II. The simulations of these angular dependences using Eq (1) and

TABLE I. Spin-Hamiltonian parameters of V_C^- in 4*H*-SiC at high temperatures. The principal *A* values are given in the unit of mT using the conversion factor of 1 mT = 28.025 MHz. The principal *x* axis of the *A*- and *g*-tensors are parallel to the [11$\bar{2}$0] direction, while the principal *y* and *z* axes are in the (11$\bar{2}$0) plane. θ is the angle between the principal *z* direction and the *c* axis given in degrees. The errors in the determination of the *g* and *A* values are ±0.0002 and ±0.03 mT, respectively. The values of $\eta^2\alpha^2$ and $\eta^2\gamma^2$ are the spin densities in the *s* and *p* orbitals, respectively. The parameters of V_C (*h*, C_{3v}) at 150 K determined in a previous study (Ref. [37]; *x* and *y* are interchanged in our coordinate) are also given for comparison.

Center	Parameters	*x*	*y*	*z*	θ	$\eta^2\alpha^2$(%)	$\eta^2\gamma^2$(%)	η^2(%)
V_C^- (*k*, C_{3v}) at 110 K								
	g	2.0035	2.0035	2.0047	0°			
	A(Si$_1$)	2.33	2.33	2.83	0°	1.5	4.1	5.6
	A(Si$_{2-4}$)	6.33	6.16	7.71	67.1°	4.1	12	16.1
	$\Sigma\eta^2$(Si$_{1-4}$)	53.9						
V_C^- (*k*, C_{3v}) at 140 K								
	g	2.0035	2.0035	2.0046	0°			
	A(Si$_1$)	2.96	2.96	3.69	0°	2	6	8
	A(Si$_{2-4}$)	6.05	5.94	7.49	69.2°	4	12.2	16.2
	$\Sigma\eta^2$(Si$_{1-4}$)	56.6						
V_C^- (*h*, C_{3v}) at 110 K								
	g	2.0038	2.0038	2.0040	0°			
	A(Si$_1$)	7.72	7.72	9.96	0°	5.2	18.3	23.5
	A(Si$_{2-4}$) not observed due to broadening							
V_C^- (*h*, C_{3v}) at 140 K								
	g	2.0038	2.0038	2.0040	0°			
	A(Si$_1$)	7.72	7.72	9.92	0°	5.2	18.0	23.2
	A(Si$_{2-4}$)	4.11	4.05	5.21	75.9°	2.7	9.4	12.1
	$\Sigma\eta^2$(Si$_{1-4}$)	59.5						
V_C^- (*h*, C_{3v}) at 295 K								
	g	2.0038	2.0038	2.0043	0°			
	A(Si$_1$)	6.95	6.95	9.06	0°	4.7	17.2	21.9
	A(Si$_{2-4}$)	4.20	4.14	5.37	76.6°	2.8	9.8	13.6
	$\Sigma\eta^2$(Si$_{1-4}$)	62.7						
V_C^- (*h*, C_{3v}) at 150 K, EPR by Umeda *et al.* (Ref. [37])								
	g	2.00381	2.00381	2.00401	0°			
	A(Si$_1$)	7.79	7.79	10.04	0°			
	A(Si$_{2-4}$)	Not observed						

the corresponding parameters are also plotted as solid curves in Fig. 7.

Using the linear combination of atomic-orbitals (LCAO) approximation, we can estimate the spin localization on Si and C neighbors of V_C^-(*k*) and V_C^-(*h*). Within the LCAO approximation, the wave function of the unpaired electron close to a neighboring Si atom can be written as a superposition of the electronic wave function (ψ_s, ψ_p) of the *s* and *p* orbitals of the Si or C atom,

$$\psi = \eta(\alpha\psi_s + \gamma\psi_p). \quad (2)$$

The localization of the wave function at a neighboring atom gives rise to hf interaction characterized by the isotropic and anisotropic components, which can be related to the unpaired spin in the *s* and *p* orbitals, respectively. The hf *A*-tensor can be decomposed into isotropic and anisotropic parts, $\mathbf{A} = a\mathbf{1} + b$, where *a* is the trace of the *A*-tensor, representing the Fermi contact, and *b* is the anisotropic part representing the dipole-dipole interaction between the electron spin and the nuclear spin of neighboring atom.[40] The *a* and *b* values

are proportional to the spin density $\eta^2\alpha^2$ in the *s* orbital and $\eta^2\gamma^2$ in the *p* orbital, respectively.

$$a = (A_{\parallel} + 2A_{\perp})/3 = (2/3)\mu_0 g\mu_B g_N \mu_N \eta^2\alpha^2 |\Psi_s s(0)|^2 \quad (3)$$

$$b = (A_{\parallel} - A_{\perp})/3$$
$$= (1/4\pi)\mu_0 g\mu_B g_N \mu_N \eta^2\gamma^2 (\pm 2/5) < r^{-3} >_p . \quad (4)$$

Here μ_N is the nuclear magneton, and g_N is the nuclear *g* value of the ^{29}Si and ^{13}C nuclei. The factor ±2/5 is the angular factor for the *p* orbital. $A_{\parallel}$ and $A_{\perp}$ are the principal values of the *A*-tensor for a defect with C_{3v} symmetry. In our case, some of the *A*-tensors have C_1 symmetry but are very close to axial symmetry, with A_X and A_Y being nearly equal. The $A_{\parallel}$ and $A_{\perp}$ values can then be approximated as $A_{\parallel} = A_z$ and $A_{\perp} = (A_x + A_y)/2$. From the isotropic and anisotropic hf parameters given by Morton and Preston,[41] the spin densities in the *s* and *p* orbitals on Si atoms can be obtained from following equations: $\eta^2\alpha^2 = a/163.93$ and $\eta^2\gamma^2 = b/4.075$ (with *a* and *b* in the unit of mT). For C atoms, the corresponding spin densities in the
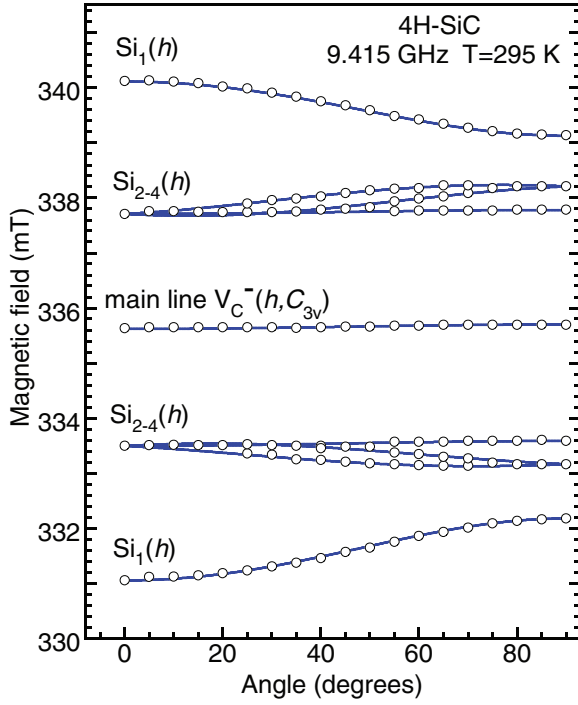
FIG. 5. (Color online) Angular dependence of the magnetic field positions of $V_C^-(h, C_{3v})$ lines (open circles) measured at 295 K with **B** rotating in the $(1\bar{1}00)$ plane. The solid curves represent the simulated angular dependence using Eq. (1) and parameters in Table I.

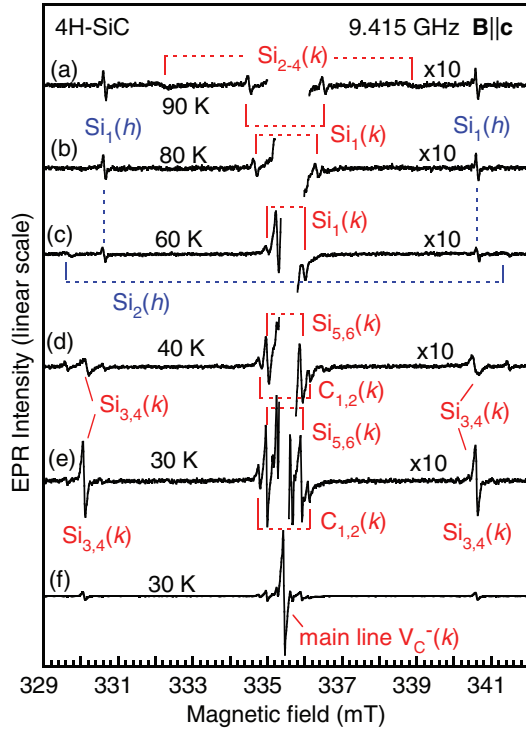FIG. 7. (Color online) Angular dependence of the magnetic field positions of $V_C^-(k)$ lines (open circles) measured at 30 K with **B** rotating in the $(1\bar{1}00)$ plane. The upper and lower parts show the angular dependence of the magnetic field positions of the $Si_{3,4}$ hf lines, while the middle part shows the corresponding angular dependence of the $C_{1,2}$ and $Si_{5,6}$ hf lines. The solid curves represent the simulated angular dependence using Eq. (1) and parameters in Table II.

s and p orbitals are $\eta^2\alpha^2 = a/134.77$ and $\eta^2\gamma^2 = b/3.832$, respectively. The obtained spin densities at Si and C neighbors of $V_C^-(h)$ and $V_C^-(k)$ at high and low temperatures are given in Tables I and II, respectively.

B. First principles simulations

1. Calculation of the hf tensors of $V_C^-(k, C_{1h})$: methodology and results

Since the present EPR data are associated with the negative carbon vacancy at the quasicubic k site in 4*H*-SiC, we determined the hf tensor of this defect by means of density functional theory (DFT) plane-wave supercell calculations. The calculation was performed with the latest version of Vienna *Ab initio* Simulation Package (VASP 5.3.3).[42,43] The all-electron projector augmented wave method (PAW)[44] was applied with plane wave basis set with standard PAW potentials provided by the VASP package. The PAW method allows accurate calculations of the spin density close to the nuclei, which is a key issue in the calculation of hf interactions.

FIG. 6. (Color online) EPR spectra in low-energy electron irradiated 4*H*-SiC measured at different temperatures for **B**∥**c** under illumination with photon energies $h\nu \sim 1.3$ eV, showing the temperature dependence of the hf structures in the range 30–90 K. The spectra in (a)–(e) are shown in ×10 intensity scale.

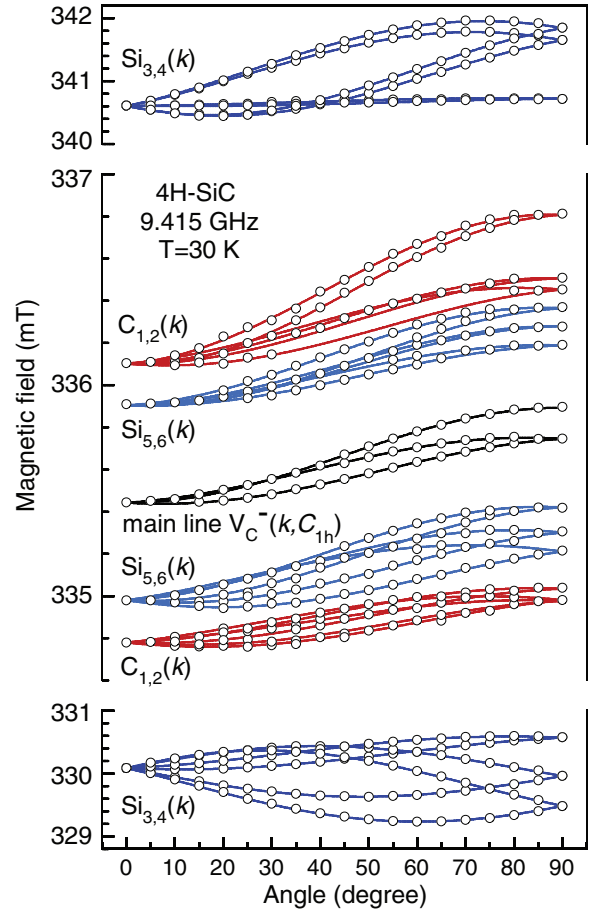TABLE II. Spin-Hamiltonian parameters of $V_C^-(k)$ determined by EPR at 30 K and calculated by supercell (576 atoms) calculations. The principal values of the hf A-tensor are given in mT using the conversion factor of 1 mT = 28.025 MHz. The polar angle θ and azimuthal angle ϕ of the principal axes of the g- and A-tensors are given in degrees. The angles $\phi = 0°$ and $\phi = 90°$ correspond to the [11$\bar{2}$0] and [1$\bar{1}$00] directions. The errors in the determination of the g and A values are ±0.0002 and ±0.03 mT, respectively. The values of $\eta^2\alpha^2$ and $\eta^2\gamma^2$ are the spin densities in the s and p orbitals, respectively. The parameters of $V_C^-(h, C_{1h})$ at 60 K determined in a previous study (Ref. 37; x and y are interchanged in our coordinate) are also given for comparison.

Parameters	x	y	z	$\eta^2\alpha^2$	$\eta^2\gamma^2$	η^2
$V_C^-(k, C_{1h})$, 30 K						
g	2.0027	2.0038	2.0054			
ϕ			90°			
θ			9.9°			
$A(\mathrm{Si}_{3,4})$	10.04	10.15	12.99	6.7	23.7	30.4
ϕ			39.0°			
θ			68.9°			
$\Sigma\eta^2(\mathrm{Si}_{3,4})$						60.8
$A(\mathrm{Si}_{5,6})$	0.87	0.85	1.12	0.6	2.1	2.7
ϕ			51.8°			
θ			62.7°			
$\Sigma\eta^2(\mathrm{Si}_{5,6})$						5.4
$A(\mathrm{C}_{1,2})$	1.33	1.31	1.85	1.1	4.6	5.7
ϕ			6.4°			
θ			82.3°			
$\Sigma\eta^2(\mathrm{C}_{1,2})$						11.4
$V_C^-(k, C_{1h})$, calculations						
$A(\mathrm{Si}_{3,4})$	9.38	9.61	12.71			
ϕ			41.0°			
θ			69.9°			
$A(\mathrm{Si}_{5,6})$	0.78	0.74	1.03			
ϕ			47.2°			
θ			63.6°			
$A(\mathrm{C}_{1,2})$	1.27	1.26	1.86			
ϕ			5.6°			
θ			82.4°			
$V_C^-(h, C_{1h})$ at 60 K, EPR by Umeda *et al.* (Ref. 37)						
g	2.00407	2.00287	2.00459			
θ			38°			
$A(\mathrm{Si}_1)$	7.76	7.76	10.07			24.1
θ			7°			
$A(\mathrm{Si}_2)$	11.67	11.78	15.19			36.6
θ			101°			
$\Sigma\eta^2(\mathrm{Si}_{1,2})$						60.7

The defect was modeled in a 576-atom supercell. Plane wave cut-off of 420 eV was used, which was sufficient to obtain convergent spin density and hf constants. The Γ-point sampling of the Brillouin zone (BZ) often provides convergent charge density in 576-atom supercell. We note that the *M* point of the BZ folds into the Γ-point in this large supercell, so the CBM of 4*H*-SiC is sampled in 576-atom supercell calculation. We will show that the sampling of CBM should be avoided in some cases, thus we also applied a 2×2×2 Monkhorst-Pack scheme.[45]

The charge and spin densities of the system was either calculated by the semilocal Perdew-Burke-Ernzerhof (PBE)[46] functional or the nonlocal, range-separated, screened hybrid Heyd-Scuseria-Ernzerhof (HSE06) hybrid functional.[47,48] We note that the calculated band gaps are 2.2 and 3.2 eV, respectively, that are to be compared to the experimental value (3.23 eV). The HSE06 functional together with the

contribution of the core spin polarization provides accurate hf tensors for well-known point defects in semiconductors, including 4*H*-SiC (Ref. 49). The optimized geometry was found by minimizing the total energy as the function of the positions of the atoms until the maximum force acting on the atoms was below 0.01 eV/Å.

We now analyze the nature of the defect states. The carbon vacancy has C_{3v} symmetry in 4*H*-SiC. Using the defect molecule model and group theory, one can obtain two nondegenerate a_1 levels and one double degenerate e level, formed by the four Si dangling bonds nearest to the vacancy. In the $V_C^-(k)$ defect, four electrons come from these dangling bonds and one extra electron from the environment that occupy the defect states. Two a_1 levels are fully occupied, while the double degenerate e level is singly occupied with a net spin of $S = 1/2$. Since the e state is only partially occupied, this system is a subject of Jahn-Teller distortion, which removes
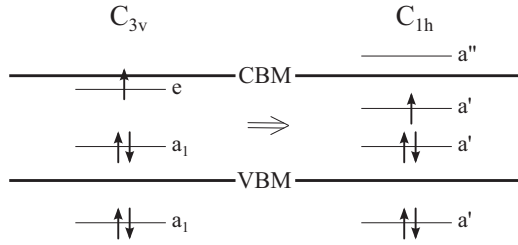
FIG. 8. Defect levels in $V_C^-(k)$. After the Jahn-Teller distortion the double degenerate e level splits to a' and a'' levels. The unpaired electron occupies the symmetric a' level, which has lower energy than the asymmetric a'' level. One of the a' levels lie in the valence band, and the other two are in the band gap, whereas the empty a'' sits in the conduction band.

the degenerate state. As a consequence, the symmetry reduces from C_{3v} to C_{1h}, so the e level splits into a' and a'' levels, as depicted schematically in Fig. 8.

We found two possible C_{1h} distortions, which result in very different spin density distribution, as shown in Figs. 9(a) and 9(b). In the stable configuration [Figs. 9(a) and 9(c)], the spin density is localized on two Si atoms in the basal plane [$Si_{3,4}$ in Fig. 9(a)]. In the metastable configuration [Figs. 9(b) and 9(d)], the spin density is localized on an Si_1 atom along the c axis and on the Si_2 atom in the basal plane [Fig. 9(b)]. We note here that PBE calculations with Γ-point sampling produce false results because only the metastable structure can be obtained with this method. The stable configuration does not form irrespective of the initial geometry in the optimization
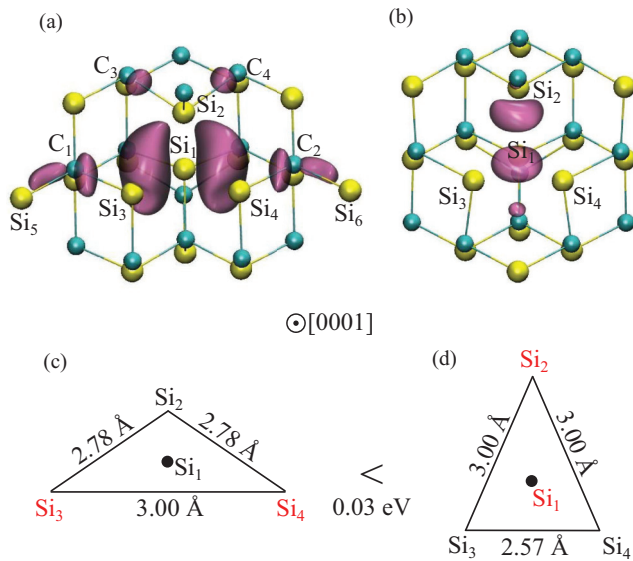

FIG. 9. (Color online) Spin densities for stable (a) and metastable (b) configurations from top view. The silicon and carbon atoms are depicted as yellow (bright) and cyan (dark) balls, respectively. The isovalues are 0.0225 1/Å for the stable geometry and 0.0630 1/Å for the metastable geometry. The distances between the silicon atoms in the basal plane corresponding to the stable (c) and metastable (d) geometries are also shown from top view. The relative stability between the two configurations is indicated. On the red (light grey) silicon atoms high spin density was obtained.

procedure due to the band gap error in the PBE functional, which artificially mixes the relatively shallow acceptor state with the conduction band states. PBE calculations with a $2 \times 2 \times 2$ MP-set can reduce this mixing because the CBM is not sampled in this k-point set; thus, the band gap is enlarged. Consequently, the appropriate stable state was found. In HSE06 calculations, the Γ-point sampling already yields the appropriate stable and metastable configurations. PBE with a $2 \times 2 \times 2$ MP-set and HSE06 Γ-point calculations both show that the energy difference between the stable and metastable configurations is only 0.03 eV. At low temperatures (~ 30 K in the experiment), the stable configuration predominantly occurs, and the corresponding spin density is detected in the EPR spectrum. In this stable configuration, the spin density is mostly localized on two, symmetrically equivalent Si atoms in the basal plane, and a measurable hf signal is expected on two symmetrically equivalent C and Si atoms among the second and third nearest-neighbor atoms, respectively. The calculated hf tensors (both the magnitude and the direction of the principal axes of the hf tensors) agree very well with the experimental data (see Table II). At elevated temperatures, the metastable state starts to dominate; thus, the spin density is transferred toward the Si atom along the c axis (Si_1) and the third Si atom in the basal plane (Si_2), where increasing temperature results in larger hf splitting on Si_1. In addition, by assuming a low energy barrier between the three symmetrically equivalent configurations of each single C_{1h} distortions (Fig. 10), these three configurations will be equally occupied both in the stable and metastable states. In other words, the static Jahn-Teller system goes to a dynamic Jahn-Teller system while showing an effective C_{3v} symmetry, and a prominent ^{29}Si hf signal can be measured along the c axis, as observed in EPR experiments for $V_C^-(k, C_{3v})$ at high temperatures.

In summary, the properties of $V_C^-(k)$ and its calculated hf tensors agree well with the experimental data. With the existence of the small barrier (~ 30 meV) between the metastable and stable state, one can explain the temperature dependence of the main EPR line and their hf satellites. All these features show the conclusive identification of the new EPR center as the $V_C^-(k)$ defect in 4H-SiC.

2. Calculation of the charge transition levels: assessment of charge correction in the supercell formalism on the acceptor level of carbon-vacancy defect in 4H-SiC

According to the EPR measurements, the observation of negative carbon vacancies in 4H-SiC requires illumination, which is explained by the negative-U property of the defect.[21,38] The detection of these signals in darkness is possible only in high-doped and highly irradiated samples at high temperatures. This is a typical behavior for a negative-U defect. In the normal case of a positive-U center, capturing another electron leads to the increase of the energy of the system due to Coulomb repulsion. In some cases, the energy gain associated with electron pairing in the dangling bonds of a defect and coupled with a large lattice relaxation might overcome the Coulomb repulsion of the two electrons, resulting in a net effective attractive interaction between the electrons at the site (a negative correlation energy U or negative U).[50] Since Z_1/Z_2 centers contain two negative-U centers
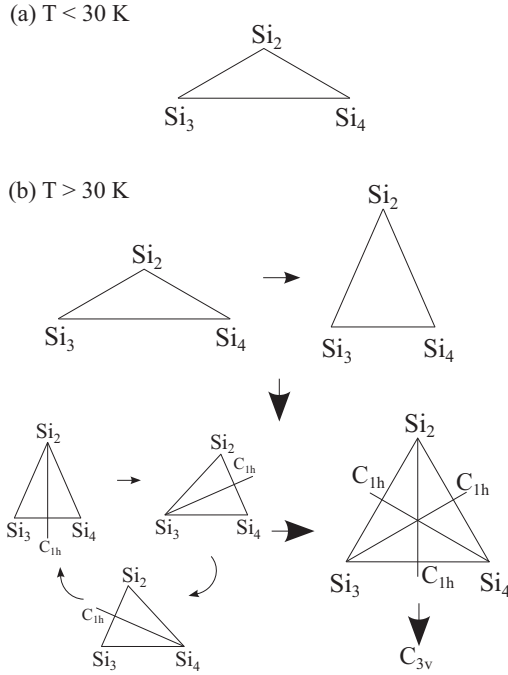
FIG. 10. Schematic sketch of the configurations of the negatively charged carbon vacancy at the quasicubic site $V_C^-(k)$ in 4*H*-SiC from top view: description of the transition from static Jahn-Teller distortion to the dynamic one as a function of temperature. (a) At lower temperatures, only the stable state exists with static Jahn-Teller distortion with C_{1h} symmetry. (b) At elevated temperatures, the metastable state will also occur beside the stable state. In the case of the metastable state, high spin density was observed on the silicon atom located along the *c* axis (not shown here: see Si_1 in Fig. 9) and one of the silicon atoms in the basal plane. Assuming low barrier energy between the symmetrically equivalent C_{1h} configurations, the spin density can be high on any of the silicon atoms in the basal plane. That is, the C_{1h} plane will rotate, resulting in an averaged C_{3v} symmetry at higher temperatures.

associated with the inequivalent substitutional sites of the C vacancy,[38] intimate inspection of the experimental conditions and data combined with the simulation results makes it possible to characterize Z_1 and Z_2 centers individually. This investigation can further support the assignment of the most efficient carrier killer Z_1/Z_2 centers with the isolated carbon vacancy in 4*H*-SiC (Refs. 21 and 38). To this end, the adiabatic charge transition levels of the acceptor levels of the carbon vacancy should be calculated and compared to the experimental data.

Principally, the adiabatic charge transition levels can be calculated within the framework of DFT supercell method. By neglecting the temperature effects, the formation energy of the carbon-vacancy defect (E_{form}) in the charge state q may be calculated by the following formula,

$$E_{form}(q) = E_{tot}(q) - n_C \mu_C - n_{Si} \mu_{Si} - q E_F, \qquad (5)$$

where $E_{tot}(q)$ is the DFT total energy of the defect where μ_C (μ_{Si}) is the chemical potential of carbon (silicon) atoms with n_C or n_{Si} number of carbon or silicon atoms in the system, and E_F is the Fermi level with respect to the calculated energy position of the valence band maximum (VBM) in the perfect supercell. For the carbon vacancy this formula is further

simplified,

$$E_{form}(q) = E_{tot}(q) - E_{tot}^{perfect} + \mu_C - q E_F, \qquad (6)$$

where E_{tot} "perfect" is the DFT total energy of the perfect supercell. If $\mu_C = \mu_C^{(b)}$ condition is set, then it corresponds to the formation energy of the defect in the extreme limit of carbon-rich condition, where $\mu_C^{(b)}$ is the calculated chemical potential of perfect diamond crystal. In this case, the formation energies of the carbon vacancies at *h* and *k* sites in neutral charge states are 5.05 eV and 4.93 eV, respectively. In the introduction, low formation energies were predicted by previous study with local density approximation or local spin density approximation,[19,20] and indeed, our results with HSE06 show that V_C can be activated thermally. We note that our HSE06 formation energies are valid at extreme C-rich conditions, while they should be a few tenths of eV smaller in real SiC crystals with carbon atoms in excess. In our particular example, q may be equal to 0, −1, or −2, when the acceptor charge transition levels of the carbon vacancy are considered. The charge transition occurs between two different charge states ($q|q+1$) under thermal equilibrium when the formation energy of two different charge states ($q+1$ and q) are the same, i.e., $E_{form}(q) = E_{form}(q+1)$. By combining this with Eq. (6), the following simple equation is obtained for the condition of charge transition,

$$E_F = E_{tot}(q+1) - E_{tot}(q). \qquad (7)$$

Thus, the charge transition level ($q|q+1$) occurs at the position of the Fermi level in the band gap of semiconductors, as imposed by Eq. (7), and the final result depends on (i) the calculated DFT VBM of the perfect supercell and (ii) the DFT total energy difference of variously charged supercell. Both issues represent a problem. The reference potential in a perfect supercell and a defective supercell is generally different; thus, the calculated VBM in the perfect supercell may not correspond to that in the defective supercell. The alignment of the average electrostatic potential of the systems may resolve this issue. A more severe problem is the treatment of charged supercell, i.e., the charge correction problem. Since the total energy of a purely charged supercell would be infinite, a compensating uniform background charge is applied, i.e., the jellium model. However, the periodic images of the charge and the compensating uniform background charge can interact with each other by Coulomb interaction where the leading term goes as $\sim 1/L$, where L is the linear size of the supercell. Thus, this interaction slowly decays with increasing the supercell size. Makov and Payne introduced a formula[51] on how to correct the total energy of atoms or molecules in supercells where the leading monopole term goes with q^2/L. This formula can be applied for charged point defects in supercells where the monopole term of the Makov-Payne formula is divided by the dielectric constant of the host material. We note that if the defect was multiple charged then the energy correction becomes very significant. This *a posteriori* correction does not depend on the nature of the defect state, and the applicability of this uniform correction might be questionable. The appropriate charge correction technique is still under intensive research.[51–57] Freysoldt and coworkers introduced such a correction scheme, which

only depends on the self-consistent electrostatic potential of the defective supercell.[55] This method assumes that the electrostatic potential can be well divided into short and long range parts, where the short range part is induced by the defect and should go to zero far from the defect in the supercell. Lany and Zunger suggested a simpler scheme[54] where they found that after the average potential alignment two-thirds of the Makov-Payne monopole correction provides convergent results as the function of the size of the supercell. They claimed that the experimental two-thirds factor can account for the compensation of the monopole correction by the quadrupole and higher order terms. The connection between these last two correction methods are given in Ref. [57]. Generally speaking, the different schemes can be monitored by scaling tests,[52,53] where the calculated formation energies are plotted as function of the size of the supercell. In a recent study, the choice of the dielectric constant in the Makov-Payne formula as well as the average potential alignment was discussed.[56] Interestingly, it has been very recently reported that none of the existing charge correction methods can uniformly provide appropriate results: when the defect state hybridizes with the band edges, all the correction schemes fail.[57]

We calculated the acceptor charge transition levels of carbon vacancies in $4H$-SiC. As the possible negative-U property occurs between $q = 0$ and $q = -2$, it is very critical to calculate the charge transition levels with an accuracy of about 0.04 eV in order to make the direct comparison with the experiments possible. As explained above, this accuracy is difficult to achieve due to the charge correction problem. We carried out a scale test for Lany-Zunger and Freysoldt charge correction schemes on the carbon vacancy in $4H$-SiC using 128-atom, 576-atom, 1944-atom, and 3200-atom supercells with full geometry optimization. We applied PBE functional in this case because the huge computer load prohibits us to use hybrid functionals. Interestingly, we found that the Lany-Zunger correction goes together with the Freysoldt correction (see Supplemental Material in Ref. [58]), as predicted in Ref. [57], We found that the 128-atom supercell is apparently too small to embed this defect, and it is inaccurate for the Freysoldt-scheme, as the short range of the electrostatic potential does not decay to zero in the boundaries (see Supplemental Material in Ref. [58]). In the 576-atom supercell, this potential almost decays perfectly, while it is perfect in the 1944-atom supercell. Since the 128-atom supercell may be too small to take into account in the scale test, we also used a giant 3200-atom supercell. Another important observation is that the results depend on the choice of those points in the supercell that are taken into account to align the average potential of the systems. This leads to an ambiguity beyond the required accuracy (0.04 eV). For instance, in the 3200-atom supercell with the $q = -2$ charge state of the carbon vacancy at the quasicubic site, if the electrostatic potential on the atoms farthest from the defect site is considered, then the difference with respect to that of the supercell is about -0.07 eV. However, if every atomic site except for the defect core region is taken into account, then this energy difference is about -0.02 eV. The energy difference ($|-0.02 - (-0.07)|$ eV = 0.05 eV) multiplied with the charge of the defect is the average potential alignment. Thus, in our particular case of $q = -2$, the ambiguity in this energy difference causes an uncertainty of 0.1 eV in

the resulted average potential alignment. This uncertainty would diminish the predictive power of the simulation and would not allow studying of the negative-U property of the carbon-vacancy defect in $4H$-SiC. It has been pointed out recently[56] that the potential alignment should be taken into account for the entire supercell. We found by inspection of the Freysoldt scheme, which provides an average potential shift, that it is consistent to use the electrostatic potential at all of the atomic sites except the core region of the defect, as was suggested by Lany and Zunger.[54] Another important observation of the simulation is that the scaling does not show convergence within 0.1 eV at all. Apparently, the acceptor level of the carbon vacancy belongs to the category where the defect state hybridizes strongly with the CBM states where none of the proposed charge correction scheme works.[57] We were able to carry out these calculations at DFT PBE level, where the band gap error in PBE may lead to an artificial hybridization of these states. It is indeed true that HSE06 defect levels are farther from the CBM and the defect states a bit more localized. However, the HSE06 defect states are still relatively close to CBM states. Overall, we chose to apply only potential alignment[55] for these defect states in HSE06 calculations (unlike in our previous publication[21]), which may cause less error than to apply the proposed Lany-Zunger or Freysoldt corrections only to the charged states of the defect.

In the 576-atom HSE06 calculations, we finally obtained the following adiabatic charge transition levels: $(-|0)$ at $E_V + 2.73$ eV and $(2-|-)$ at $E_V + 2.53$ eV for $V_C(k)$, while the corresponding levels are at $E_V + 2.63$ eV and at $E_V + 2.57$ eV for $V_C(h)$, respectively. The calculated HSE06 band gap (3.16 eV) is about 0.07 eV lower than the experimental gap. Because the $(2-|-)$ levels lie deeper than $(-|0)$ levels, both sites show the negative-U property. Taking the calculated band gap, the aforementioned values correspond to $(-|0)$ at $E_C - 0.43$ eV and $(2-|-)$ at $E_C - 0.63$ eV for $V_C(k)$, whereas they correspond at $E_C - 0.53$ eV and $E_C - 0.59$ eV for $V_C(h)$, respectively. The corresponding stable $(2-|0)$ transitions can be found at $E_C - 0.53$ eV and at $E_C - 0.56$ eV for $V_C(k)$ and $V_C(h)$, respectively. These levels might be deeper because of the too low band gap; thus, the direct comparison with the experimental data should be done with a great care. Nevertheless, two trends are apparent: (i) the negative-U effect is stronger at k site than at h site, and (ii) the metastable $(-|0)$ level is closer to the conduction band at k site than at h site. We emphasize that these conclusions are correct even taking the uncertainties in the charge correction into account as any type of the proposed charge correction schemes would result in the same shifts in the charge transition levels both for $V_C(k)$ and $V_C(h)$.

In the photo-EPR study, the energy thresholds corresponding to the $(-|0)$ and $(2-|0)$ levels of $V_C(h)$ were determined at $\sim E_C - 0.74$ eV and $\sim E_C - 0.78$ eV, respectively.[38] The ordering of the levels is in line with the prediction from calculations, supporting the conclusion of the negative-U properties of V_C. Slightly larger energies in photo-EPR experiments of ~ 0.20–0.25 eV compared to the calculated values are expected since optical transitions involve also a Franck-Condon shift, which were theoretically predicted to be ~ 0.21–0.41 eV for the neutral and single negative charge

states of V_C in 4H-SiC (Ref. 59). Thus, taking into account the Franck-Condon shift in optical transitions, the previously calculated energy levels are in good agreement with the corresponding levels determined by EPR.

C. Discussion

The observation of a strong EPR signal in our samples already suggests that the associated center is related to a defect in the C sublattice since the energy of ∼250 keV electrons can create mainly C vacancies, C interstitials, and their associated complexes. The observation of a center with C_{3v} symmetry having the hf interaction between an electron spin with a nuclear spin of a ^{29}Si nucleus at one of the four nearest Si sites at elevated temperatures (∼140 K) further suggests that the defect is an isolated defect and likely a V_C. The appearance together of $V_C^-(k)$ and $V_C^-(h)$ as only two dominant EPR signals in irradiated layers naturally suggested that they belong to the same defect occupying two inequivalent lattice sites. The transition from C_{1h} to C_{3v} symmetry also occurs for the $V_C^-(k)$ center in the same temperature range, as in the case of $V_C^-(h)$. While the observation of the $V_C^-(k)$ signal is expected, the similarity in parameters compared to $V_C^-(h)$ provides further support for its identification as $V_C^-(k)$. As can be seen in Tables I and II, both $V_C^-(h)$ and $V_C^-(k)$ show the hf interaction with four nearest Si neighbors at high temperatures and mainly with two Si neighbors at low temperatures. The spin densities on the nearest Si neighbors are also similar for the two centers [∼56.6% for $V_C^-(k, C_{3v})$ and ∼59.8% for $V_C^-(h, C_{3v})$ at ∼140 K and ∼60.7–60.8% for both centers at low temperatures]. There is a difference in spin distribution between $V_C^-(k)$ and $V_C^-(h)$. For $V_C^-(k, C_{1h})$, the angle between the principal Z axis of the Si$_{3,4}(k)$ hf tensor and the c axis determined by EPR at 30 K is ∼68.9°, close to the angle of the basal bond (71°). Thus, the spin localization is mainly with two Si$_{3,4}$ atoms in the basal plane. The obtained hf parameters for Si$_{3,4}(k)$ are very close to that calculated for $V_C^-(k, C_{1h})$ in 4H-SiC (see Table II). The transfer of the spin density from Si$_{3,4}(k)$ in the basal plane to the Si$_1$ along the c axis predicted by calculations when the defect changes from the static Jahn-Teller system to the dynamic Jahn-Teller system at elevated temperatures due to thermal average has also been observed by EPR in the range of 80–140 K, further supporting the identification of $V_C^-(k)$. Unlike the $V_C^-(k, C_{1h})$ center, $V_C^-(h, C_{1h})$ shows the hf interaction with one Si atom along the c axis (Si$_1$) and another Si atom (Si$_2$) in the basal plane. Such spin localization in $V_C^-(h, C_{1h})$ has previously been confirmed by calculations.[37] Thus, the difference in the spin localization on the two nearest Si neighbors of $V_C^-(h, C_{1h})$ and $V_C^-(k, C_{1h})$ is also in line with the prediction from calculations. Compared with the calculations, the two Si$_{5,6}(k)$ and C$_{1,2}(k)$ hf structures, which were observed for $V_C^-(k, C_{1h})$ but have not been detected for $V_C^-(h, C_{1h})$, can also identified as due to the hf interaction of the electron spin with the nuclear spin of one ^{29}Si atom occupying one of two Si sites in the third neighbor and with one ^{13}C atom occupying two C sites in the second neighbor, respectively (see Table II). Such a good agreement in the spin-Hamiltonian parameters obtained by EPR and supercell calculations firmly supports the identification of the new EPR spectrum to be related to $V_C^-(k)$.

As mentioned in Sec. III. A, the observation of strong $V_C^-(h)$ and $V_C^-(k)$ signals requires illumination. In the low-doped sample after electron irradiation, the carbon vacancies remain in neutral charge state in darkness and are EPR inactive. Under illumination with photon energy $h\nu \geq 1.8$ eV, the electrons could be removed from neutral charge state carbon vacancies[27–29] and captured by other neutral charge carbon vacancies. Therefore, both positive charge and negative charge states of carbon vacancies could be observed by EPR. In the high-doped sample, the observation of the V_C^- signal can be explained by its negative-U properties. In this case, V_C is not stable in the single negative charge state and prefers to capture another electron to become doubly negatively charged and relaxes to a lower energy level. Thus, depending on the location of the Fermi level in n-type material after irradiation, under equilibrium and at low temperatures, V_C will be in either the neutral or double negative charge state, which are both EPR inactive and cannot be detected in darkness. Under illumination with $h\nu \sim 1.3$ eV, electrons were removed from the double negative charge state and converted a part of the total concentration of the carbon vacancies to the single negative charge state. This photon energy was not enough to activate the positive charge state carbon vacancies;[27–29] therefore, only negative carbon vacancies could be observed by EPR. In darkness, at elevated temperatures the thermal energy can excite electrons from the $(2-|0)$ level to the higher lying $(-|0)$ level, transforming a part of the total concentration of V_C from the 2− charge state to the singly negatively charged state, which can be detected by EPR. The temperature required for the observation of the V_C^- signal in darkness depends on the separation between the $(2-|0)$ and $(-|0)$ levels. Compared to $V_C^-(k)$, the $V_C^-(h)$ signal appears at lower temperatures and can be detected even in samples irradiated with lower fluences. This suggests that the separation between the $(2-|0)$ and $(-|0)$ levels is smaller for $V_C^-(h)$. Considering the system consisting of two deep levels of V_C [$(2-|0)$ and the higher lying $(-|0)$ level] and E_C, there are two processes that can change the population on the $(-|0)$ level, i.e., the concentration of V_C^-. In the first process, electrons in the $(2-|0)$ level is excited to the $(-|0)$ level, leading to the increase of the concentration of V_C^-, and, hence, its EPR signals. When thermal energies can efficiently excite electrons from the $(-|0)$ level to E_C, then the process of removal electrons from this level occurs, competing with the first process, leading to the decrease of the population on the level. The population on the $(-|0)$ level thus strongly depends on the total concentration of V_C in the 2− charge state and the separation between the two states. In low-doped n-type samples, the concentration of V_C in the 2− charge state is limited by low concentration of the N-shallow donors, resulting in too low population on the $(-|0)$ level to be detectable by EPR. This explains why only in high-doped samples the $V_C^-(k)$ and $V_C^-(h)$ signal could be detected in darkness. As shown from the temperature dependence study, the $V_C^-(k)$ signal disappeared at 250 K, whereas the $V_C^-(h)$ signal can still be detected at room temperature. This suggests that the $(-|0)$ level is shallower for $V_C(k)$. Thus, our EPR result is in line with the prediction from calculations and supports the assignment of the energy levels of different charge states of

$V_C^-(k)$ and $V_C^-(h)$ in the previous EPR and DLTS study:[38] the (2−|0) level is related to the Z_1/Z_2 level at $\sim E_C - (0.56/0.71)$ eV, and the (−|0) levels of $V_C(h)$ and $V_C(k)$ are related to the higher lying Z_1 and Z_2 levels of the negative-U Z_1/Z_2 defect at $\sim E_C - 0.52$ eV and $\sim E_C - 0.45$ eV, respectively. The *ab initio* simulation supports these conclusions. The calculated (−|0) levels of $V_C(h)$ and $V_C(k)$ are at $E_C - 0.53$ eV and $E_C - 0.43$ eV, respectively, which agrees with the experimental results. We also found that the separation between (2−|0) and (−|0) levels is smaller for $V_C^-(h)$ than for $V_C^-(k)$, which is in line with the interpretation of the experimental data. By this comparison, the DLTS fingerprints of the individual carbon vacancies are identified in our study.

IV. SUMMARY

In summary, we have shown that V_C is the dominating defect in low- and high-doped *n*-type 4*H*-SiC freestanding epilayers irradiated by low-energy (250 keV) electrons. Using high-doped *n*-type samples irradiated on both sides, we could detect the EPR spectra of V_C^- at both inequivalent lattice sites in 4*H*-SiC without the interference from the signals of the N shallow donors and the V_C^+ center. The Si and C ligand hf structures of both centers have been studied by EPR in a wide temperature range from 30 K to room temperature, providing strong experimental evidences supporting the identification of V_C^- at the quasicubic site, $V_C^-(k)$-the center that has not been observed before. The identification of $V_C^-(k)$ is further

confirmed by our supercell calculations of the hf constants of the hf interactions between the electron spin and the nuclear spins of ^{29}Si and ^{13}C atoms at the first, second, and third neighbor shells of the vacancy. At low temperatures, the spin density on the nearest Si neighbors was found to be similar for $V_C^-(k, C_{1h})$ (~60.8%) and $V_C^-(h, C_{1h})$ (~60.7%) but with different distribution (mainly on two Si atoms in the basal plane for $V_C^-(k, C_{1h})$ and on one Si atom along the *c* axis and another Si atom in the basal plane for $V_C^-(h, C_{1h})$). Both $V_C^-(k)$ and $V_C^-(h)$ are characterized by an electron spin of 1/2 in a Si-Si antibonding state of the vacancy, undergoing a large lattice relaxation to form a negative-U system. The experimental and simulation results support the previous assignment of deep levels of the Z_1/Z_2 defect to the double and single acceptor levels of the negative-U system of V_C, and the individual sites of the carbon vacancy are identified.

*gali.adam@wigner.mta.hu

†son@ifm.liu.se

[1] M. Bhatnagar and B. J. Baliga, IEEE Trans. Electron Devices **40**, 645 (1993).

[2] A. Elasser and T. P. Chow, Proc. IEEE **90**, 969 (2002).

[3] H. Lendenmann, F. Dahlquist, J. P. Bergman, H. Bleichner, and C. Hallin, Mater. Sci. Forum **389**, 1259 (2002).

[4] J. Zhang, L. Storasta, J. P. Bergman, N. T. Son, and E. Janzén, J. Appl. Phys. **93**, 4708 (2003).

[5] T. Tawara, H. Tsuchida, S. Izumi, I. Kamata, and K. Izumi, Mater. Sci. Forum **457**, 565 (2004).

[6] P. B. Klein, B. V. Shanabrook, S. W. Huh, A. Y. Polyakov, M. Skowronski, J. J. Sumakeris, and M. J. O'Loughlin, Appl. Phys. Lett. **88**, 052110 (2006).

[7] J. R. Jenny, D. P. Malta, V. F. Tsvetkov, M. K. Das, H. McD. Hobgood, C. H. Carter, Jr., R. J. Kumar, J. M. Borrego, R. J. Gutmann, and R. Aavikko, J. Appl. Phys. **100**, 113710 (2006).

[8] K. Danno, D. Nakamura, and T. Kimoto, Appl. Phys. Lett. **90**, 202109 (2007).

[9] T. Dalibor, G. Pensl, H. Matsunami, T. Kimoto, W. J. Choyke, A. Schöner, and N. Nordell, Phys. Status Solidi A **162**, 199 (1997).

[10] T. Kimoto, A. Itoh, H. Matsunami, S. Sridhara, L. L. Clemen, R. P. Devaty, W. J. Choyke, T. Dalibor, C. Peppermüller, and G. Pensl, Appl. Phys. Lett. **67**, 2833 (1995).

[11] L. Storasta, J. P. Bergman, E. Janzén, A. Henry, and J. Lu, J. Appl. Phys. **96**, 4909 (2004).

[12] K. Danno and T. Kimoto, J. Appl. Phys. **100**, 113728 (2006).

[13] C. G. Hemmingsson, N. T. Son, A. Ellison, J. Zhang, and E. Janzén, Phys. Rev. B **58**, R10119 (1998); **59**, 7768 (1999).

[14] C. Hemmingsson, N. T. Son, O. Kordina, J. P. Bergman, E. Janzén, J. L. Lindström, S. Savage, and N. Nordell, J. Appl. Phys. **81**, 6155 (1997).

[15] L. Storasta and H. Tsuchida, Appl. Phys. Lett. **90**, 062116 (2007).

[16] T. Miyazawa and H. Tsuchida, J. Appl. Phys. **113**, 083714 (2013).

[17] T. Hiyoshi and T. Kimoto, Appl. Phys. Express **2**, 041101 (2009).

[18] T. Hiyoshi and T. Kimoto, Appl. Phys. Express **2**, 091101 (2009).

[19] A. Zywietz, J. Furthmüller, and F. Bechstedt, Phys. Rev. B **59**, 15166 (1999).

[20] L. Torpo, M. Marlo, T. E. M. Staab, and R. M. Nieminen, J. Phys.: Condens. Matter **13**, 6203 (2001).

[21] T. Hornos, A. Gali, and B. G. Svensson, Mater. Sci. Forum **679**, 261 (2011).

[22] N. T. Son, P. N. Hai, and E. Janzén, Phys. Rev. B **63**, 201201 (2001).

[23] T. Umeda, J. Isoya, N. Morishita, T. Ohshima, T. Kamiya, A. Gali, P. Deák, N. T. Son, and E. Janzén, Phys. Rev. B **70**, 235212 (2004).

[24] N. T. Son, P. N. Hai, and E. Janzén, Mater. Sci. Forum **353**, 499 (2001).

[25] V. Ya. Bratus, I. N. Makeeva, S. M. Okulov, T. L. Petrenko, T. T. Petrenko, and H. J. von Bardeleben, Physica B **308**, 621 (2001).

[26] V. Ya. Bratus', T. T. Petrenko, S. M. Okulov, and T. L. Petrenko, Phys. Rev. B **71**, 125202 (2005).

[27] N. T. Son, B. Magnusson, and E. Janzén, Appl. Phys. Lett. **81**, 3945 (2002).

[28]J. Dashdorj, M. E. Zvanut, and J. G. Harrison, J. Appl. Phys. **104**, 113707 (2008).

[29]P. Carlsson, N. T. Son, F. C. Beyer, H. Pedersen, J. Isoya, N. Morishita, T. Ohshima, and E. Janzén, Phys. Stat. Sol. RRL **3**, 121 (2009).

[30]M. E. Zvanut and V. V. Konovalov, Appl. Phys. Lett. **80**, 410 (2002).

[31]N. T. Son, B. Magnusson, Z. Zolnai, A. Ellison, and E. Janzén, Mater. Sci. Forum **433-436**, 45 (2003).

[32]N. T. Son, B. Magnusson, Z. Zolnai, A. Ellison, and E. Janzén, Mater. Sci. Forum **457-460**, 437 (2004).

[33]P. Carlsson, N. T. Son, B. Magnusson, A. Henry, and E. Janzén, Mater. Sci. Forum **600-603**, 381 (2009).

[34]N. T. Son, P. Carlsson, J. ul Hassan, B. Magnusson, and E. Janzén, Phys. Rev. B **75**, 155204 (2007).

[35]A. Ellison, B. Magnusson, N. T. Son, L. Storasta, and E. Janzén, Mater. Sci. Forum **433-436**, 33 (2003).

[36]St. G. Müller, M. F. Brady, W. H. Brixius, R. C. Glass, H. McD. Hobgood, J. R. Jenny, R. T. Leonard, D. P. Malta, A. R. Powell, V. F. Tsvetkov, S. T. Allen, J. W. Palmour, and C. H. Carter, Jr., Mater. Sci. Forum **433-436**, 39 (2003).

[37]T. Umeda, Y. Ishitsuka, J. Isoya, N. T. Son, E. Janzén, N. Morishita, T. Ohshima, H. Itoh, and A. Gali, Phys. Rev. B **71**, 193202 (2005).

[38]N. T. Son, X. T. Trinh, L. S. Løvlie, B. G. Svensson, K. Kawahara, J. Suda, T. Kimoto, T. Umeda, J. Isoya, T. Makino, T. Ohshima, and E. Janzén, Phys. Rev. Lett. **109**, 187603 (2012).

[39]K. Kawahara, X. T. Trinh, N. T. Son, E. Janzén, J. Suda, and T. Kimoto, Appl. Phys. Lett. **102**, 112106 (2013).

[40]J. A. Weil and J. R. Bolton, in *Electron Paramagnetic Resonance-Elementary Theory and Practical Applications*, second ed. (John Wiley & Sons, Inc., Hoboken, New Jersey, 2007), p. 121.

[41]J. R. Morton and K. F. Preston, J. Magn. Res. **30**, 577 (1978).

[42]G. Kresse and J. Hafner, Phys. Rev. B **49**, 14251 (1994).

[43]G. Kresse and J. Furthmüller, Phys. Rev. B **54**, 11169 (1996).

[44]P. E. Blöchl, Phys. Rev. B **50**, 17953 (1994).

[45]H. J. Monkhorst and J. D. Pack, Phys. Rev. B, **13**, 5188 (1976).

[46]J. P. Perdew, K. Burke, and M. Ernzerhof, Phys. Rev. Lett. **77**, 3865 (1996).

[47]J. Heyd, G. E. Scuseria, and M. Ernzerhof, J. Chem. Phys. **118**, 8207 (2003).

[48]A. V. Krukau, O. A. Vydrov, A. F. Izmaylov, and G. E. Scuseria, J. Chem. Phys. **125**, 224106 (2006).

[49]K. Szász, T. Hornos, M. Marsman and A. Gali, Phys. Rev. B **88**, 075202 (2013).

[50]P. W. Anderson, Phys. Rev. Lett. **34**, 953 (1975).

[51]G. Makov and M. C. Payne, Phys. Rev. B **51**, 4014 (1995).

[52]A. Gali, T. Hornos, N. T. Son, E. Janzén, and W. J. Choyke, Phys. Rev. B **75**, 045211 (2007).

[53]C. W. M. Castleton, A. Höglund, and S. Mirbt, Phys. Rev. B **73**, 035215 (2006).

[54]S. Lany and A. Zunger, Phys. Rev. B **78**, 235104 (2008).

[55]C. Freysoldt, J. Neugebauer, and C. G. Van de Walle, Phys. Rev. Lett. **102**, 016402 (2009).

[56]S. E. Taylor and F. Bruneval, Phys. Rev. B **84**, 075155 (2011).

[57]H.-P. Komsa, T. T. Rantala, and A. Pasquarello, Phys. Rev. B **86**, 045112 (2012).

[58]See Supplemental Material at http://link.aps.org/supplemental/10.1103/PhysRevB.88.235209 for additional data about scale tests on the charged defective supercells.

[59]M. Bockstedte, A. Marini, O. Pankratov, and A. Rubio, Phys. Rev. Lett. **105**, 026401 (2010).